A molecular investigation on lignin thermochemical conversion and carbonaceous organics deposition induced catalyst deactivation★

Cheng Chen [1], Roberto Volpe [1], Xi Jiang [1]*

[1] School of Engineering and Materials Science, Queen Mary University of London, Mile End Road, London E1 4NS, UK

*Corresponding author. Email: xi.jiang@qmul.ac.uk

Abstract

Surface coking is the primary deactivation pattern of metal-based catalyst in biofuel reforming, which hinders the commercial utilisation of biomass. In this study, molecular dynamics simulation with reactive force field is performed to investigate the surface instability induced thermal degradation of Ni nanocatalyst and coke deposition induced catalyst deactivation. Coke deposited on catalyst surfaces is a complex mixture of carbonaceous organics. Coke surrogate models containing polycyclic aromatic hydrocarbons (PAHs) and oxygenated aromatics are proposed to reflect the molecular size and O/C ratio based on the molecular structures identified during lignin pyrolysis and soot inception mechanism. Lindemann index is used to characterize the degree of crystallinity of catalyst. It is found that atoms at unsaturated sites of outer shell show high mobility and tend to modify the coordination number distribution. Mechanisms behind the effects of temperature, PAH size and oxygen content on coke adsorption are revealed from three aspects of molecular collision dynamics, thermal dynamics and kinetics. The modification of crystallinity of catalyst outer shell and the occurrence of seeping after coke adsorption would affect the subsequent catalyst regeneration. This study is expected to provide guidance on the design of anti-coking catalyst, evaluation of catalyst regeneration and reactor optimisation.

Key words: biomass, catalyst deactivation, coke deposition, molecular modelling

★ The short version of the paper was presented at ICAE2020, Dec 1-10, 2020. This paper is a substantial extension of the short version of the conference paper.

1 Background

In order to achieve carbon neutrality and meet the requirement of 2°C scenario, biofuel consumption is projected to triple and account for 9% of global transportation fuel demand by 2030 as conceived in the Sustainable Development Scenario (SDS) roadmap [1]. Consumption share of advanced biofuels derived from lignocellulosic biomass such as agricultural and forestry wastes is expected to further scale up substantially considering sustainability of lignocellulose and massive production of 170 billion metric tons per year [2]. On the other hand, current biofuel output trend can hardly reach the anticipated steady annual growth rate of 10% required by SDS [1]. Accelerated deployment of biofuel production is needed, which particularly depends on innovative technologies to reduce energy conversion costs and improve efficiencies, as well as facilitate the commercialisation of advanced biofuels.

Among the process technologies, thermochemical conversion is more suitable for industry-scale utilisation compared with the biochemical methods, *e.g.*, anaerobic and aerobic digestion [3]. Lignocellulose comprising of cellulose, hemicellulose and lignin can be cracked and depolymerized rapidly into biofuels during pyrolytic degradation at elevated temperature. Gasification is also promising and commonly used in treatment. Syngas produced from the gasification of biomass can be used as fuels directly after purification or synthesized into high-value-added chemicals like ethanol and dimethylether However, biocrude liquid fuel is a complex mixture containing aromatics, phenolics, acids, hydroxyketones, *etc*. The number of oxygenated compounds in a typical biofuel can be over 300 during biomass pyrolysis, resulting in undesirable attributes of high viscosity, low energy content and corrosiveness [4]. Tar formation is the main issue in gasification that can clog the downstream equipment, increase the maintenance cost and hinder biomass utilisation. Tars formed inevitably during gasification refer to a series of condensed organics from single ring aromatics like toluene to heavy polycyclic aromatic hydrocarbons (PAHs) of 4-7 rings. Oxygenated aromatics like dibenzophenol also exists [5]. It is acknowledged that catalyst can play a significant role in both biofuel reforming and tar removal.

By adding appropriate catalyst like base transition metal nanoparticles into the reactors, the desirable reaction pathways can be selectively enhanced, leading to the biomass valorisation and thus achieving the optimization of the products. However, catalysts undergo deactivation temporally or permanently during their lifetime through a series of physicochemical phenomena [6-10]. Catalyst deactivation leads to secondary reactions, prohibiting the conversion rate and probably weakening the production of H_2 in gasification [11]. Understanding catalyst deactivation mechanisms and developing strategies to design stable catalysts are as important as research of catalytic selectivity

and activity in practice, but deactivation processes are often overlooked in academic research [12]. For industrial application, catalyst regeneration excluding irreversible deactivation can help to control the replacement costs, and thus make the reforming process more favourable. Bartholomew [13] classified the deactivation mechanism into six types, *i.e.*, poisoning, fouling, sintering, crushing, catalyst surfaces reacting with gas to produce volatile compound, and inactive phase formation on catalyst surfaces after reaction with vapour, support or promoter. In terms of biofuel/tar reforming, coke deposition is the most notorious and the primary deactivation mechanism [4, 6, 14]. Surface coking inhibiting active sites from being available for reaction is affected by many factors, including the composition of feedstock and operating conditions like temperature, pressure and contact time, *etc*. Arregi *et al*. [15] studied the deactivation rate of nickel (Ni) supported catalyst in in-line steam reforming. It was observed that the increasing concentration of non-reformed oxygenated phenolic compounds in reaction medium accelerated the deactivation. Ochoa *et al*. [16] showed that coke morphology mainly affected by temperature also caused a deep impact on deactivation of Ni. It was also observed that coke deposition and evolution result in dragging and reduction of the size of Ni particles in ethanol steam reforming [17, 18].

Modelling plays a key role in understanding catalyst deactivation mechanisms, facilitating the process optimization, and thus promoting commercialization of biofuels [19-21]. Classical molecular dynamics (MD) simulation provides an opportunity to study the three-dimensional structure of biomass components and quantification of their interactions at nanoscale level [22, 23]. For example, MD simulation with all-atom force fields demonstrated the effect of hydrogen bonding on strength of crystalline cellulose nanofiber [24]. Using coarse grained force field, Lindner *et al.* [25] studied the aggregation of lignin on the surface of cellulose chains in aqueous solution with the system size of 3.8 million atoms. Owing to the capability in predicting thermophysical properties and describing diffusion process in complex pores of zeolites, MD simulation can also contribute to the reactor design [26-28]. In addition to the experimental methods like thermogravimetric (TG) analysis to study biomass pyrolysis, MD with reactive force field (ReaxFF) enables the modelling of breaking and forming of chemical bonds and so as to identify elementary pathways and the associated kinetic parameters of macromolecular architecture of biomass [29, 30]. Batuer *et al*. [31] developed a ReaxFF MD simulation model of cotton cellulose pyrolysis in both non-isothermal and isothermal conditions. It was found that 80% and 100 % of volatile removal ratios was the closest to the TG experimental results. The work of Monti *et al.* [32] showed that the ReaxFF simulation of lignin fragmentation on a Pd catalyst was capable of revealing the surface chemistry details of adsorption dynamics of reactive oligomer and deposition dynamics of the generated fragments.

Although significant experimental work has been performed on coke deposition induced catalyst deactivation taking place in biomass pyrolysis and upgrading, further fundamental modelling studies is required to deepen the understanding of the physiochemical phenomena. This would help to optimise the processing condition and attenuate deactivation. To the best of our knowledge, ReaxFF MD modelling of catalyst surface coking in biomass utilisation has not been carried out. In this study, the coke surrogate models are proposed firstly based on the distribution of lignin pyrolysis products and soot inception mechanism. Nanocatalyst surface premelting induced thermal degradation is studied *via* Lindemann index and atom displacement magnitude. A ReaxFF MD simulation system is established to elucidate the deactivation mechanism by demonstrating the time evolution of catalyst morphology and interactions with coke, to reveal the effect of coke size, O/C ratio and operating temperature on chemisorption/physisorption. Afterwards, the deactivation extent of catalyst is quantified *via* adsorption ratio and relative Lindemann index over a wide range of conditions.

2 Modelling methodology

2.1 Computational method

In this study, all MD simulations are performed using ReaxFF force field where all connectivity dependent interactions are described based on bond order formalism. Bond order determined by interatomic distance using an empirical formula is continuous and includes contributions from σ, π and $\pi\pi$ bonds. By updating bond order at every iteration, ReaxFF MD method is able to model the bond formation and dissociation. Nonbonded terms like van der Waals and Coulomb interaction are calculated independently. Charge equilibration (QEq) method is used to adjust the partial charge on individual atoms based on interactions with their neighbours. System energy associated with different forces on each atom is calculated using the following equation:

$$E_{system} = E_{bond} + E_{over} + E_{under} + E_{lp} + E_{val} + E_{tor} + E_{vdWaals} + E_{coulomb} \quad (1)$$

where E_{bond}, E_{over}, E_{under}, E_{lp}, E_{val}, E_{tor}, $E_{vdWaals}$, and $E_{coulomb}$ represent bond energy, overcoordination energy penalty, undercoordination stability, lone pair energy, three-body valence angle energy, four-body torsional angle energy, van der Waals energy, and Coulomb energy, respectively. In this study, the latest developed C/H/O parameter set [33] was used to study lignin pyrolysis, as it improved the C1 chemistry and was widely applied to describe reaction network and kinetics during pyrolysis and oxidation of syngas, phenoxy-aromatic fuels, multicomponent diesel *etc.* [33-35]. C/H/O/Ni parameter set [36, 37] developed for modelling hydrocarbon chemistry catalysed by Ni was adopted to study the surface coking over Ni nanocatalysts.

2.2 Model construction

Lignin is the third major component of lignocellulose, accounting for 10-35% by weight, up to 40% by energy in biomass [2]. Compared with semi-crystalline polysaccharide cellulose and amorphous polysaccharide hemicellulose, lignin is an amorphous aromatic polymer composed of three basic monomer units, *i.e.*, p-hydroxyphenyl (H), guaiacyl (G) and syringyl (S) as shown in **Fig. 1(a)**. The proportion of H, G and S units in lignin strongly depends on the biomass species. The exact molecular structure of lignin is difficult to characterize. The linkages of basic lignin units are complex and mainly include C-O ether bonds (β-O-4, α-O-β', γ-O-4, α-O-γ', and α-O-4 *etc*) and C-C bonds like α-6 as shown in **Fig. 1(b)**. In this study, a simplified softwood lignin structure containing seven most common linkages proposed by Beste was adopted [38].

As one of the most promising active phases, Ni is widely used in reforming process [6]. In this study, face-centred cubic (fcc) lattice of Ni nanoparticles as shown in **Fig. 1(c)** was created on a web-based crystallographic tool [39]. The minimum surface energy of corresponding Miller indices of (111), (100) and (110) was adopted from the work of Jiang *et al.* [40]. In order to study the surface premelting phenomena, Ni catalyst is divided into three layers, *i.e.*, layer1 (L1) atom identities (IDs) range from 1 to 369; IDs of L2 range from 370 to 1229; IDs of L3 range from 1230 to 2867.

Coke is always referred to as any unwanted carbonaceous organics depositing on the catalyst surfaces, and varies in composition depending on the reforming temperature and resident time. It is generally classified into different types based on morphology or structure, *e.g.*, highly oxygenated encapsulating coke and aromatic filamentous coke [6, 16]. In order to simplify the complex coke composition and better understand the adsorption and decomposition mechanisms on the catalyst surfaces, surrogate coke molecular models are proposed as shown in **Fig. 1(d)**. Peri-condensed PAHs including naphthalene (A2), pyrene (A4), coronene (A7), ovalene (A10), circumcoronene (A19) which are constituted of 2-, 4-, 7-, 10-, and 19-numbered aromatic rings respectively, are selected to represent a large range of molecular size. These PAH monomers are regarded as the key precursors and building blocks in soot formation of incomplete hydrocarbon combustion, and used widely to study the nucleation and condensation mechanism in soot inception [41, 42]. The counterparts of phenolic compounds including phenol (A1O1), hydroquinone (A1O2), phloroglucinol (A1O3) and benzenehexol (A1O6) are selected to reflect the effect of O/C ratio.

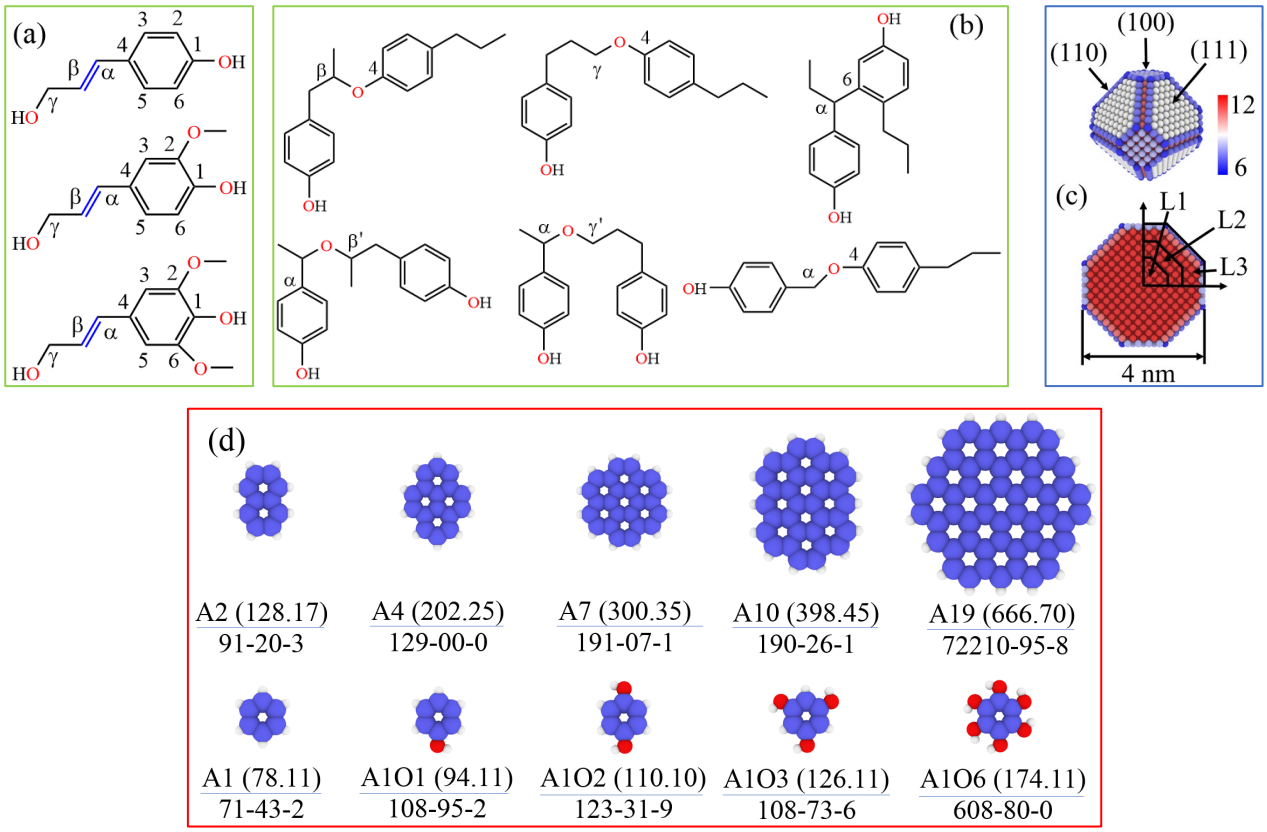

Fig. 1. (a)-(b): Basic units of lignin and various linkage in the lignin structure; (c) atom arrangement of a 4 nm Ni nanocrystal in tridimensional view with facets indicated and the cross section with different layers (L1, L2 and L3) indicated, the atoms are coloured according to the coordination number (CN) with cut off distance of 3.2 Å; (d) molecular structures of coke surrogate models with molecular structure, molecular weight and CAS number indicated, H atom coloured in grey, C atom coloured in blue and O atom coloured in red.

2.3 Simulation setup procedures and details

For lignin pyrolysis simulation, 40 lignin unimolecules containing 13720 atoms are constructed into a 200 × 200 × 200 Å cubic box with a lower initial density to avoid overlapping of major functional groups. After system energy minimisation, the box is further compressed using an isobaric-isothermal NPT (fixed atom numbers, pressure, and temperature) ensemble at 300 K and 100 bar with a time step of 0.25 fs until the density reduced to 1.25 g/cm^3, which is close to the value in the work of Zhang *et al.* [43]. Thereafter, to relax the system, 3 recycle simulation in NPT ensemble at atmospheric pressure with temperature annealing between 300 K and 400 K was performed for 100 ps, followed by isochoric-isothermal NVT (fixed atom numbers, volume, and temperature) simulation at 400 K for 100 ps. The equilibrated system with a 51.1 × 51.1 × 51.1 Å cubic box is shown in **Fig. 2(a)**. Production run is continued using canonical NVT ensemble from the equilibrated system, ramping from 300 K to 3000 K with the heating rate of 20 K/ps.

Both non-isothermal and isothermal simulations are set up using canonical NVT ensemble with the Ni nanocrystals placed in the centre of a 100 × 100 × 100 Å cubic box as shown in **Fig. 2(b)** to investigate the melting process of nanocatalyst. Nonisothermal simulation is performed first to study the dynamic melting with the temperature ramping from 300 K to 3000 K in 500 ps simulation. Separate isothermal simulation is then performed to study the equilibrium melting process using constant temperatures from 400 K to 2400 K with temperature interval of 400 K.

For simulation of coke deposition, each of the coke surrogate molecule is duplicated 50 times and distributed randomly into the 100 × 100 × 100 Å cubic box with a 4 nm Ni nanocatalyst fixed in the centre as exhibited in **Fig. 2(c)**. Isothermal simulation of 800 ps with time step of 0.25 fs is performed using canonical NVT ensemble. The trajectories and species information are outputted at every 400 steps. The linear and angular momentum of Ni nanocrystal is zeroed every 10 time steps.

The periodic boundary condition is applied in all directions. The velocity of molecules is assigned according to Maxwell-Boltzmann distributions of the specified temperature. The Nosé-Hoover thermostat and barostat are adopted to control the system temperature and pressure with a temperature and pressure damping constant equal to 100 times and 1000 times of the time step respectively. A bond order cut off of 0.3 is employed to recognize the molecules and analyse the species forming during the simulation. The ReaxFF MD simulation is performed with REAXC package in the Large-scale Atomic/Molecular Massively Parallel Simulation (LAMMPS) [44]. All the visualizations are produced by OVITO [45].

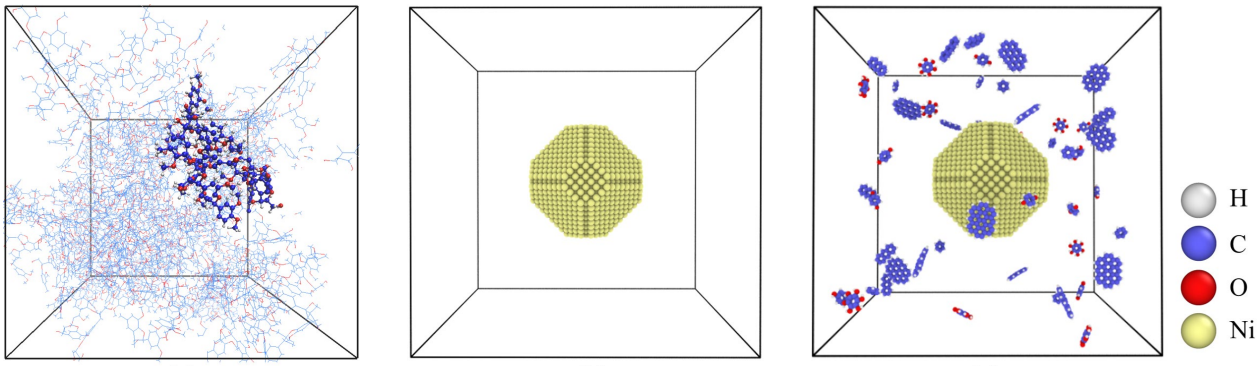

Fig. 2. (a) Snapshot of the equilibrated unit cell with one unimolecular ($C_{138}H_{160}O_{45}$) of the 40 lignin fragments highlighted; (b) 4 nm Ni nanocrystal centred in the box for modelling of catalyst thermal stability; (c) schematic box depicting the modelling system of coke adsorption, Ni catalyst is fixed in centre with aromatic organics distributed around.

3 Results

3.1 Lignin pyrolysis products

Nonisothermal simulation is performed first to study the lignin mass fraction change during pyrolysis and is compared with our TG experimental results of kraft lignin as shown in **Fig. 3**. Based on the species evolution in **Fig. 3(a)**, the lignin pyrolysis processes can be roughly summarized into three stages. Pyrolysis at temperatures ranging from 300 K to 800 K is the initial stage where lignin molecules mainly proceed to conformation adjustment with a slight mass loss. Very few small radicals like CH_3O, CH_3, and OH are observed in this stage. The second pyrolysis stage takes place when temperature ramps from 1000 K to 1800 K. The macromolecular lignin structure decomposes appreciably while number of species increases slightly in this stage. Existence of secondary reaction at temperatures from 1800 to 3000 K results in the apparent increase of species in the last pyrolysis stage. It should be pointed out that although there is a temperature difference between the experiment (423-1173 K) and simulation (800-3000 K), pyrolysis process is described well in the ReaxFF MD simulation following the consistent decreasing trend from the simulation and TG experiment as shown in **Fig. 3(a)**. Relevant work [31, 46, 47] also verified the elevated temperature strategy used in ReaxFF MD can well reproduce the pyrolysis mechanism of coal, cellulose and oil shale kerogen at higher experimental temperatures.

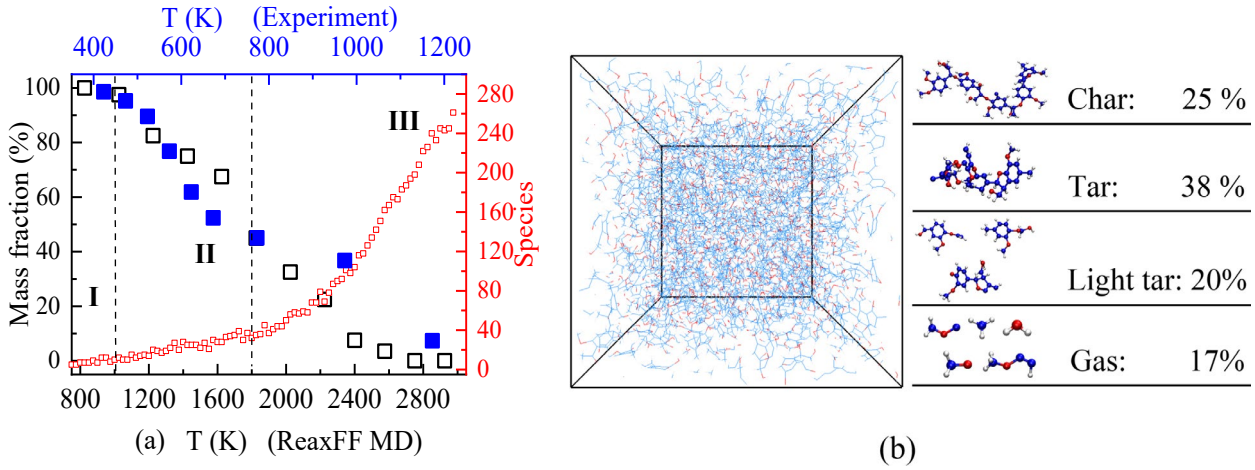

Fig. 3. (a) Evolution of lignin mass fraction and number of species where blue solid box is mass fraction of TG experiment (temperature ramp: 2 K/min), black hollow box is mass fraction of ReaxFF MD simulation (20 K/ps), red hollow box is species of ReaxFF MD simulation; (b) snapshot of the system and the mass fraction of final composition yield, typical molecular structures are identified.

Depending on the degree of pyrolysis, the lignin macro molecular structures depolymerize into volatile compounds, monomers, oligomers, and solid bio-char. Pyrolysis products are generally

classified as char, heavy tar, light tar and gases according to molecular size [31]. Compounds containing more than 40 carbon atoms are considered as char as shown in **Fig. 3(b)**. Fragments including 14-40 carbon atoms and 5-13 carbon atoms are considered as heavy tar and light tar which account for 38% and 20%, respectively. The gas molecules accounting for 17% of the products include organic gases containing 1-4 carbon atoms and inorganic gases like H_2, CO_2 and H_2O *etc*. The oxygenated aromatics composition of tar can sustain for long duration even under supercritical conditions and is supposed to proceed to dehydration leading to the formation of aromatic compounds such as benzene, toluene and xylenes [48]. These coke precursors can further pyrolyze and polymerize *via* H-Abstraction-Carbon-Addition (HACA) soot inception mechanism [3, 49], facilitating the formation of condensed heavy PAH. For example, naphthalene, which is also recognized as the most stable and difficult-to-decompose compound among biomass-derived tars, is selected as the surrogate model to study the catalyst deactivation in tar reforming [7, 11, 14].

3.2 Surface instability induced thermal degradation

Temperature is recognised as the most common factor resulting in metal sintering during steam reforming processes. The dynamic melting temperature (T_m) of nanocrystal of different sizes can be obtained by the time evolution of the average potential energy (*pe*) using nonisothermal temperature ramping simulation as shown in **Fig. 4(a)**. The melting behaviour of the 4 nm crystal is further characterized using the atom distribution function $g(r)=4\pi r^2\rho dr$ as shown in **Fig. 4(b)**. It describes local number density (ρ) variation as a function of distance (r) from a reference atom, and can reveal the structural information of local order degree. The *pe* curves mainly pass through three stages, taking 4 nm crystal as an example. In the first stage, a gradual linear increase of *pe* is seen between 400 K to1550 K. The corresponding curves of $g(r)$ display a series of well-defined peaks at time before 240 ps, indicating that long-range ordered structure and crystalline arrangement are well preserved. When temperature is higher than 2000 K, *i.e*., after 320 ps, melting enters the third stage where the *pe* still increases linearly with temperature with a higher slop, while long-range order of atom distribution function vanishes indicating the completely amorphous liquid phase. The nonlinear sharp increase region between 1550 K and 2000 K is related to the solid-to-liquid transition, where 2000 K is always regarded as the melting point of the system as indicated by the dash lines in **Fig. 4(a)**. The melting temperature depends strongly on size, and a linear decrease in melting temperature is found with increasing reciprocal of radius as shown in **Fig. 4 (c)**. The melting temperature of bulk nickel is obtained by extrapolating $1/R \rightarrow 0$ is 2512 K which is about 40 % higher than the experimental value of 1728 K.

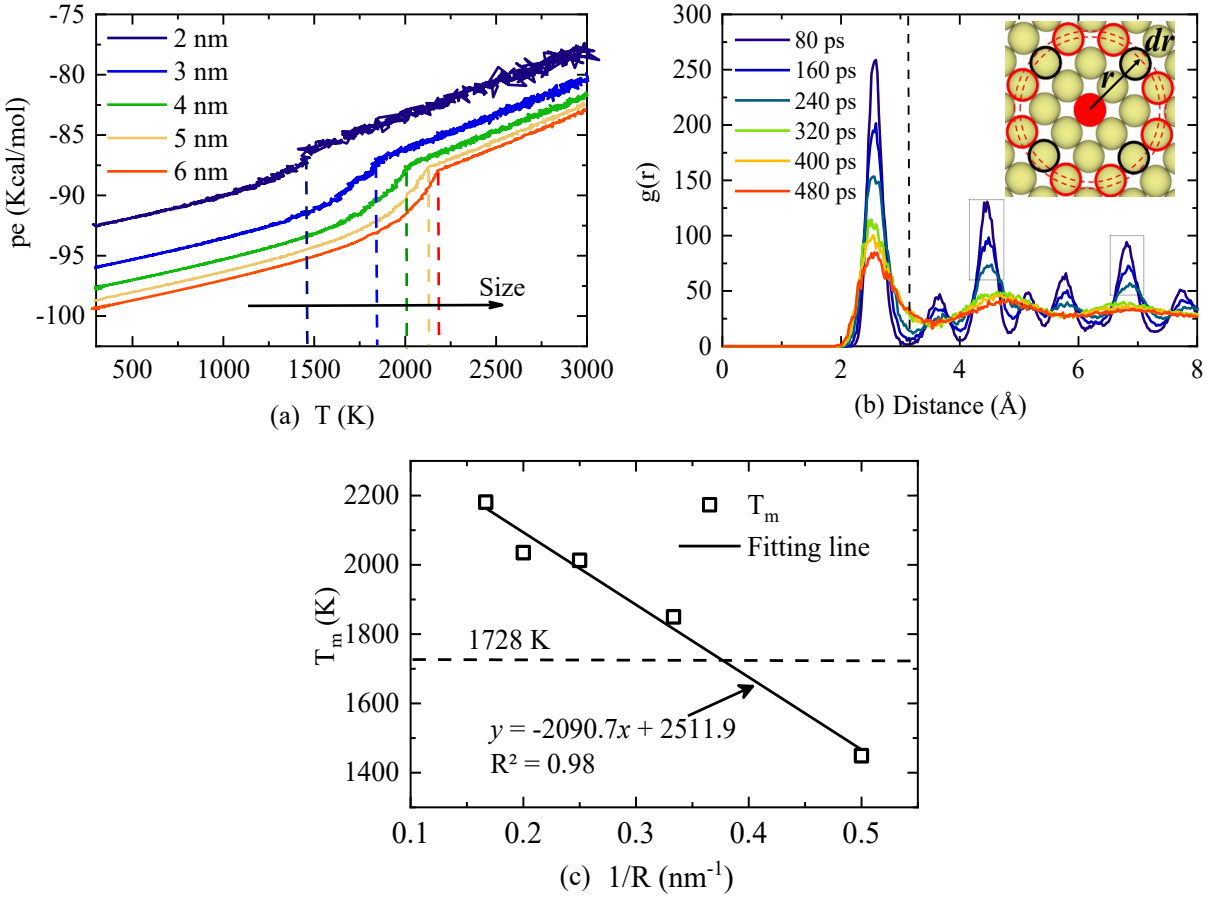

Fig. 4. (a) Potential energy per atom of nanocrystal with diameters of 2-6 nm heating from 300 K to 3000 K; (b) time evolution of the radial distribution function of the 4 nm nanocrystal heating from 300 K to 3000 K in 500 ps; (c) melting temperatures of Ni crystal with different sizes determined by potential energy evolution.

In order to eliminate the effect of insufficient equilibrium during the temperature ramp, a number of isothermal simulations were performed. Dimensionless Lindemann index representing the degree of atomic vibration is employed to quantify the crystallinity of nanoparticles. The Lindemann index is defined as:

$$\delta_i = \frac{1}{N-1}\sum_{j\neq i}\frac{\sqrt{\left\langle r_{ij}^2\right\rangle_T - \left\langle r_{ij}\right\rangle_T^2}}{\left\langle r_{ij}\right\rangle_T} \tag{2}$$

$$\delta = \frac{1}{N}\sum_i \delta_i \tag{3}$$

where δ_i is the Lindemann index of the ith atom, δ is the system-averaged value, N is the number of atoms in nanocrystal, r_{ij} is the interatomic distance between atom i and j, $\langle\cdots\rangle_T$ denotes the time average at temperature T. The Lindemann index of 4nm nanocrystal at different temperatures is shown in **Fig. 5(a)**. It is known that the catalyst reactivity is closely related to the number of the nearest

neighbours of the surface atom, *i.e.*, coordination number. The coordination number distribution of the Ni nanocrystal shown in **Fig. 1(c)** is determined using the first minimum of the atom distribution function, *i.e.*, 3.2 Å as the cut-off distance. The distribution of coordination number of outer shell at different temperatures is presented in **Fig. 5(b)**.

Phase change of Ni nanocrystal during melting is determined at the temperature where Lindemann index δ increases to 0.08 [50]. High Lindemann index denotes high vibrational motion of atoms and disordered structural morphology. The bulk melting temperature predicted using Lindemann index as the criterion in ReaxFF MD simulation is 2298 K, still 33% higher than the experiment result but closer to that from the potential energy method. It is also observed that a sudden increase of Lindemann index takes place in L3 outer shell at 1600 K which corresponds to the drastic change in coordination number distribution in **Fig. 5(b)**, while inner layers of L1 and L2 still persevere ordered solid state at 1600 K. Surface disordering before complete melting is regard as a general phenomenon during nanocrystal melting due to the existence of the unstable undercoordinated atoms with dangling bonds as indicated in **Fig. 1(c)**. The higher values of the potential energy per atom in both solid and liquid states for the smaller nanocrystals in **Fig. 4(a)** are a reflection of the increased fraction of loosely bounded surface atoms.

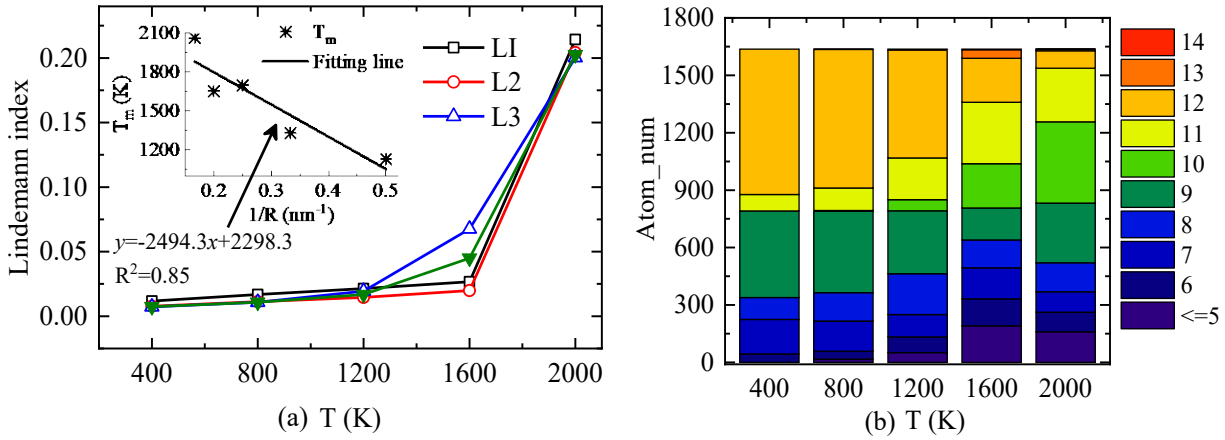

Fig. 5. (a) Lindeman index of 4 nm nanocrystal at isothermal conditions, the melting temperature of different sizes based on Lindemann index criteria is inserted, the solid triangle is the result of nanocrystal; (b) distribution of coordination number of L3 surface at different isothermal conditions.

It is believed that strict surface melting phenomenon defined with the formation of quasi-liquid film occurs only if the radius of nanocrystals is larger than the critical value (*e.g.*, 2.96 nm for Ni [51]). Surface structure instability induced deactivation of 4 nm crystal is scrutinised, considering that even slight atom modifications in crystal surfaces can affect activity and selectivity in catalysis. Generally, when temperature reaches Hüttig temperature ($0.3T_m$, *i.e.*, around 689 K), the surface

atoms located at corners, steps, and terraces with reduced coordination numbers tend to dissociate and diffuse readily over the surface. After temperature further approaches to Tamman temperature ($0.5T_m$, *i.e.*, around 1149 K), the bulk atoms start to show mobility [49]. The melting behaviours are reflected *via* displacement magnitude as shown in **Fig. 6**. The surface atoms show apparent mobility at 1200 K with the average displacement magnitude of outer shell almost 3 times greater than the core layer. The atoms with prominent mobility, *i.e.*, those with deviation displacement from lattice position greater than 3.2 Å, present mainly at junction edges or corners of facets. These atoms also account for 39% of the out shell at 1600 K, explaining the drastic change in coordination number distribution. At temperatures of 2000 K and 2400 K, the nanocrystal becomes totally amorphous, indicating frequent change of atoms between different layers.

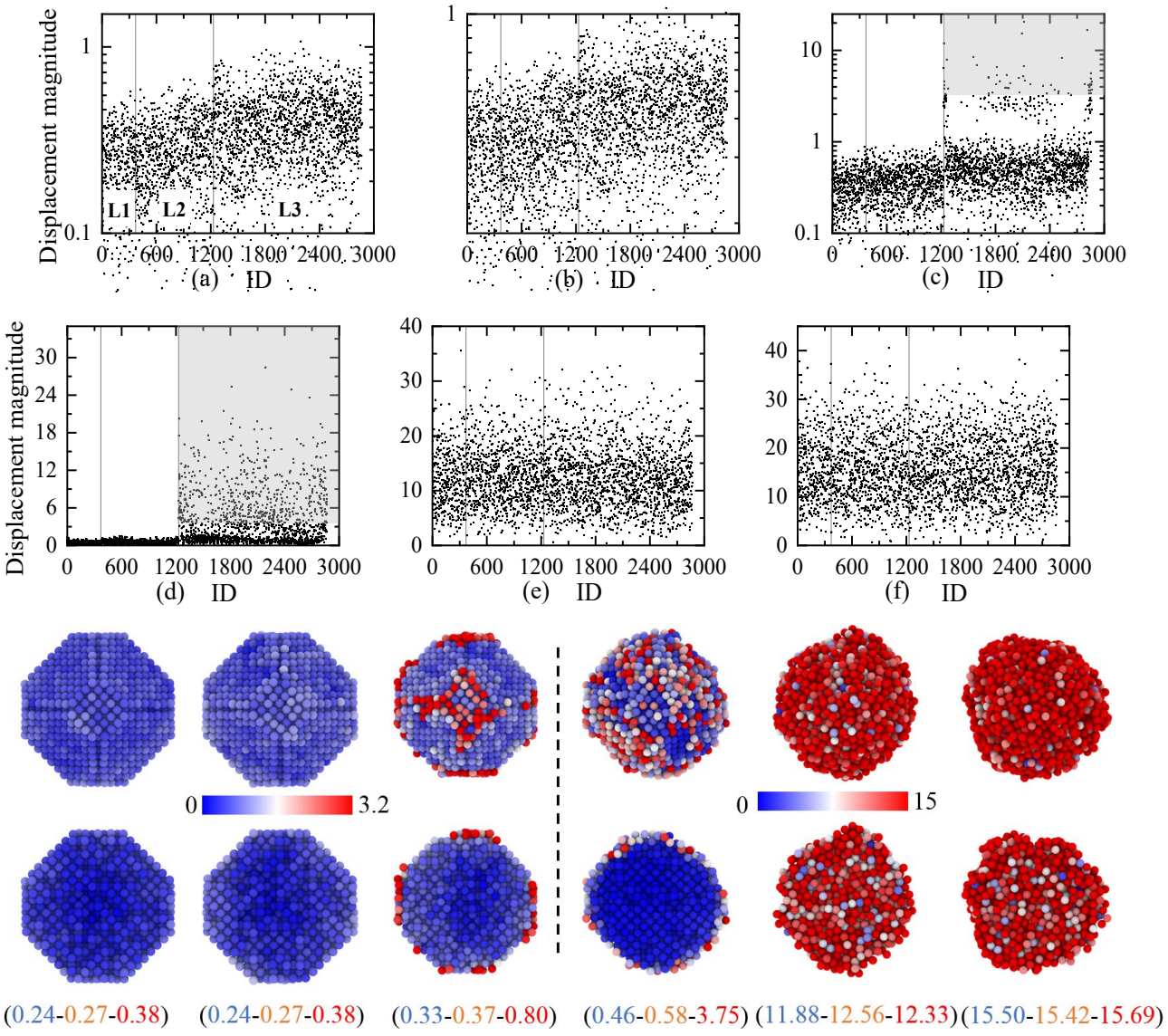

Fig. 6. Scatter plots of displacement magnitude along with atom ID of 4 nm nanocrystal at different time and the corresponding coloured maps of the overall and cross sectional snapshots; (a)-400 K, (b)-800 K, (c)-1200 K, (d)-1600 K, (e)-2000 K, (f)-2400 K; the numbers in bracket indicates displacement magnitude

of different layers, blue-L1, orange-L2, red-L3; grey area in (c) and (d) indicates atoms with displace over 3.2 Å.

3.3 Deposition induced deactivation

Carbonaceous molecular adsorption onto catalyst surfaces is the first step to study coke deposition induced deactivation, involving coke composition, operating temperature and reaction time. In order to decouple these factors, isothermal ReaxFF MD simulation using the proposed aromatic coke surrogate molecules (see **Fig. 1(d)**) at 1200 K was performed to investigate the time evolution of adsorption process as illustrated in **Fig. 7**. Corresponding snapshots to depict the key stages during adsorption are displayed in **Fig. 8**. Temperature effects on adsorption ranging from 400 K to 2000 K are confined to typical molecules of benzene (A1, minimum aromatic size), pyrene (A4, medium size PAH), circumcoronene (A19, maximum size PAH) and benzenehexol (A1O6, the highest oxygen content), as illustrated by the snapshots in **Fig. 9**. Time evolution of molecules is obtained in ReaxFF MD simulation through the dumped information of molecular quantities and chemical formulas of species identified by the bond order criteria of 0.3. It should be noted that except for the plane-parallel monolayer adsorption onto Ni facets (**Fig. 8(b-1)**), the addition of PAH stacks with various misalignment and conformation onto Ni surfaces is also frequently observed (**Fig. 9**). The analysis of the overall adsorption is extended to the recognition of the new cluster comprising Ni nanocrystal and the adsorbates. Here, an interatomic distance criteria of 4 Å adopted from the work of Qian *et al.* [41], which has been used to distinguish physical nucleation PAH clusters, is employed as illustrated in **Fig. 7(a)**. The adsorption ratio is thereof defined as the proportion of the adsorbate atoms. From **Fig. 7(b)-(e)**, the effects of molecular size and O/C ratio on time evolution of adsorption tendency in different stages are elaborated into four aspects: initial adsorption rate, binding stability, decomposition of adsorbates and final adsorption ratio.

For benzene (A1), adsorption ratio fluctuates appreciably in all the simulation time with a low final adsorption ratio of 25%, and the number of benzene molecules reduces steadily to 35. It should be pointed out that PAH monomer constructed ReaxFF MD systems are observed to be chemically stable at 1200 K [41], and there is no decomposition occurring in our homogenous test system of A1O6 in the absence of Ni nanocatalyst. This indicates that the reduction of aromatic molecules is entirely due to the surface reaction after adsorption. We display two typical interaction scenarios between benzene and nanocrystal in **Fig. 8(a)** and **(b)**. The first type is that benzene is trapped at the time of 15 ps, and desorbed back immediately after 7 ps surface diffusion. Trap-diffusion-desorption is regarded as void-collision leading to the unstable physisorption which accounts for the fluctuation in adsorption ratio. The second type is that benzene diffuses on the surface for almost 399 ps after trapped by nanocrystal

until decomposition occurs, *e.g.*, dehydrogen forming C_6H_5 and aromatic ring opening. Trap-diffusion-decomposition is regarded as effective-collision, in which situation, adsorbates are able to reside on the surface for a long period due to the tuned energy exchange and momentum accommodation with the particle [52].

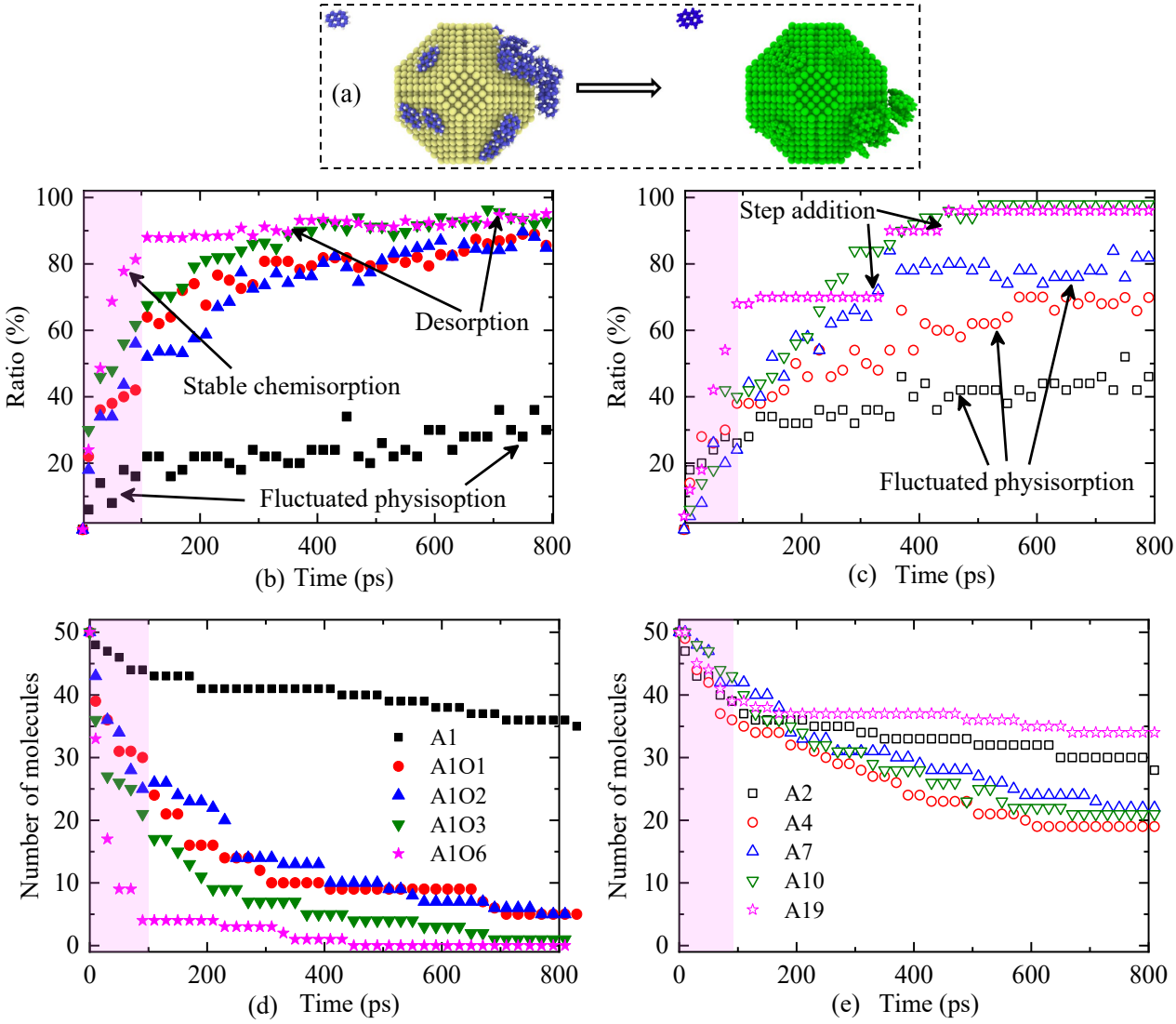

Fig. 7. (a) Schematic plot of the cluster recognition (coloured by green) with a cut off distance of 4 Å; (b)-(c): time evolution of overall adsorption ratio; (d)-(e): time evolution of the number of aromatic molecules; magnitude coloured area is initial stage of A1O6 and A19.

Comparing the adsorption ratios, it is observed that medium size PAHs (A2, A4 and A7) show heavier fluctuation while step addition occurs in large size PAHs (A10 and A19) in the late stage. This is because only A10 and A19 undergo thermally stable physical nucleation forming PAH stacks at 1200 K [41]. The A19 trimers are subsequently trapped as a whole onto the aromatic subtracts at the time of 452 ps (**Fig. 8(c)**), accounting for the 6% increase of adsorption ratio (**Fig. 7(c)**). Also, it should be noted that 1200 K is the transition point for dimerization of A10. Thus, step addition of

A10 is not as prominent as A19 and most A10 is monolayer adsorbates. The reduction of A10 is much more than A19 considering that PAH nucleation stacks result in the multi-layered adsorbates. This is described as PAH nucleation induced physisorption. A19 has the highest initial adsorption rate, and larger PAH has higher final adsorption ratio for medium PAHs, indicating that large PAH size enhances effective collision.

Aromatics with higher oxygen contents show higher initial adsorption rate and lower fluctuation (**Fig. 7(b)**). This indicates that oxygen in coke also facilitates effective collision. The substituent hydroxyl group in the benzene can lower decomposition activation energy and enhance the decomposition rate (**Fig. 7(d)**). After adsorption, benzenehexol can proceed to the surface reaction like C-O bond fission, O-H bond fission and ring opening *etc.* (**Fig. 8(d)**). The radicals can further react into H_2O which can then desorb back into the gas phase (**Fig. 9(d-3)**), thus result in the low fluctuation of the adsorption ratio.

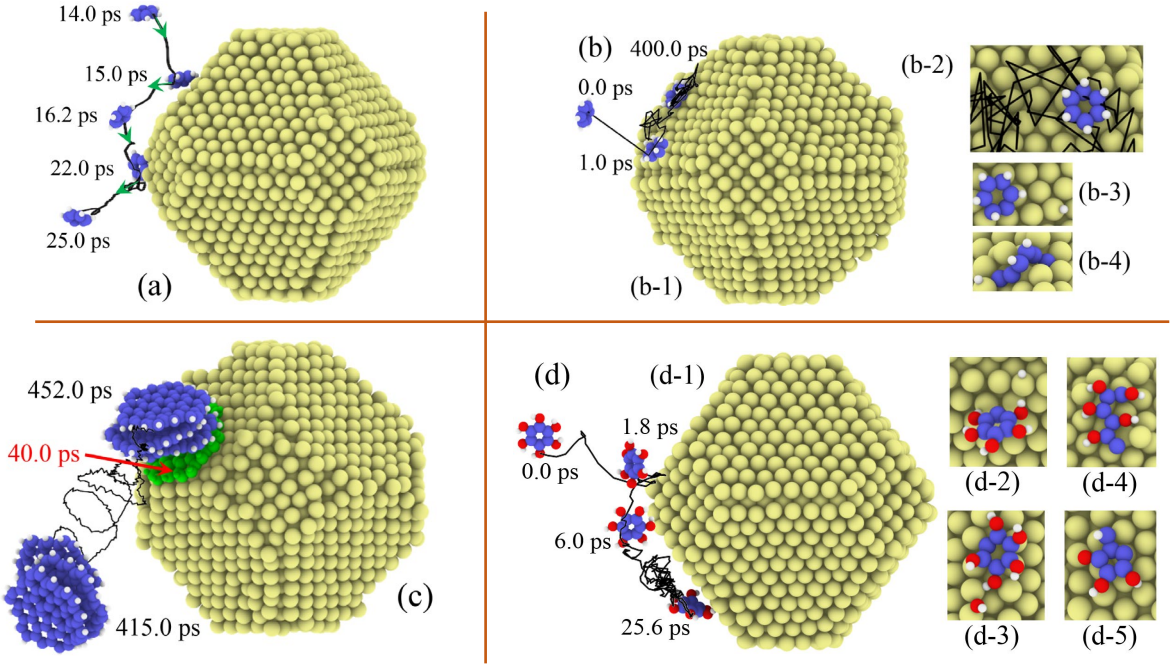

Fig. 8. Representative trajectories (black lines) to show the time evolution of aromatic molecular interaction with the surfaces of Ni nanocrystal; (a)-(b): A1, (c): A19 and (d): A1O6; green arrow in (a) indicates the movement direction of A1; (b-2) is the modified view of (b-1) to indicate the diffusion trajectory of A1 on (111) facet, (b-3) and (b-4) are part of the products after surface reaction; A19 in (c) coloured in green is trapped at the time of 40 ps and acted as subtracts for PAH stack adsorption; (d-2) to (d-5) are typical products captured after surface reaction.

Through the above analysis, it can be revealed that the mechanism of coke adsorption onto the catalyst surface includes three aspects: molecular collision dynamics, thermal dynamics and kinetics. Although both dynamics and kinetics undoubtedly depend on temperature, the effects of temperature

on adsorption of different coke surrogate molecules in **Fig. 9** become complicated particularly when coupled with binding energy type between the adsorbates and the substrate, *i.e.*, physisorption by weak van der Waals forces and chemisorption by covalent bonds. To be specific, at conditions where there is no surface reaction occurring, *e.g.*, at 400 K and 800 K, the binding energy between A1O6 and Ni surface is covalent bond as the cluster is recognised as a molecule with the formula of $Ni_{2867}C_{300}H_{300}O_{300}$. This also explains that higher oxygen content facilitates effective collision. However, the binding energy is observed to depend on the posture for PAHs, *i.e.*, only aromatic rings parallel to the catalyst surface and binding through the C-C π orbitals are identified as covalent bonding.

A1 adsorption ratios at 400 K, 800 K and 1200 K are 98%, 38% and 30% respectively. The velocity of molecules in MD accords with the Maxwell-Boltzmann distribution, *i.e.*, $v_p=(2RT/M)^{1/2}$, where v_p is the most probable velocity, R is the gas constant and M is molar mass of the substance. A higher temperature is supposed to lead to higher probability of void-collision in physisorption due to higher momentum and kinetic energy [52]. However, when temperature is increased further to 1600 K and 2400 K, adsorption ratio increases to 40.33% and 57.67% even though desorption occurs at 2400 K. This indicates surface reaction kinetics plays a role at high temperature. Same situation also occurs for A4, where adsorption ratio decreases from 97.20% at 800 K to 70.77% at 1200 K, while increases from 54.95% at 1600 K to 58.52% at 2000 K. For the effect of thermal dynamics, it is known that PAH dimer lifetime is sensitive to molecular size, and it decreases in elevated temperature. Physical nucleation of A4 at 400 K and A19 from 400 K to 2000 K generates the PAH stacks and results in the multi-layered adsorbates.

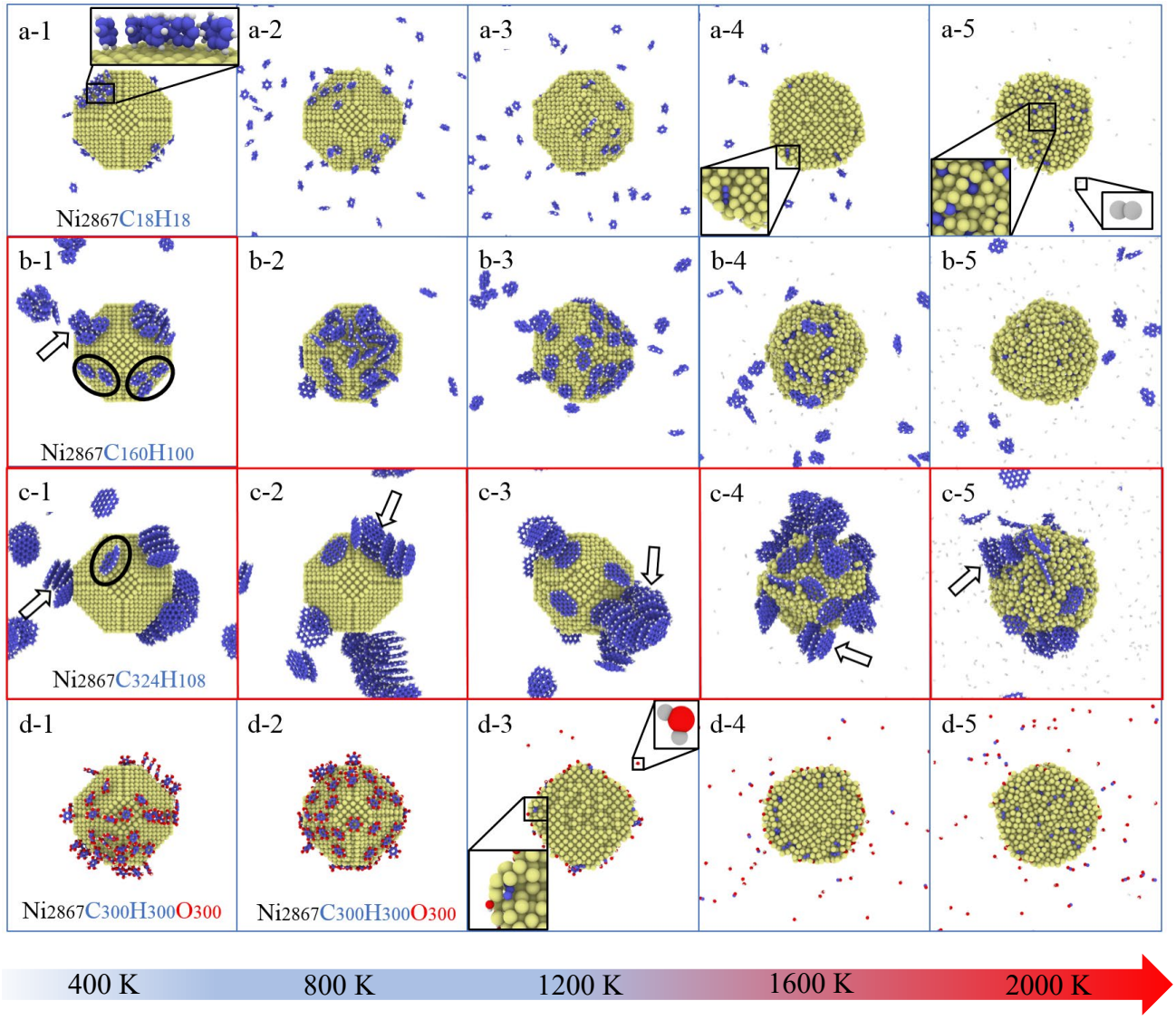

Fig. 9. Snapshots of the system after 800 ps isothermal simulation to demonstrate the temperature effect on adsorption of A1, A4, A19 and A1O6; molecular formula of the cluster in (a-1), (b-1), (c-1) and (d-1), (d-2) is indicated at the bottom of the panel; (a-4), (a-5), (d-3), (d-4) and (d-5) are cross section snapshots, and intermediates seeping into catalyst are indicated in the enlarged snapshot; PAHs with its ring parallel to the particle surface are indicated by the black circle in (b-1) and (c-1); the conditions where physical nucleation occurs according to the work of Qian *et al.* [41] are highlighted by the red frame and multi-layered adsorbates are indicated by black arrows.

4 Discussion

Catalyst deactivation due to coke deposition is usually reversible, and the surface adsorbates can easily be removed by oxidation with O_2. The degradation of catalyst crystallinity is the real concern in regeneration. We compared the Lindemann index of nanocrystal outer shell after adsorption with the corresponding isothermal melting value at the same temperature as shown in **Fig. 10**. It is clear

that PAH adsorption reduces the Lindemann index at 1200 K and above, indicating more ordered crystalline structure than isothermal melting. It is assumed that the covalent bond between adsorbates and catalyst surface after chemisorption prohibits the mobility of crystal surface atoms, facilitating the preserve of crystallinity. Meanwhile, the effect of oxygen content is not as prominent as PAH size. However, it should be noted that when temperature was increased to 1600 K and 2000 K, seeping of the PAH surface reaction intermediates into the inner layer of catalyst occurs (see **Fig. 9**) which indicates the failure of conventional surface regeneration method that may result in the irreversible deactivation.

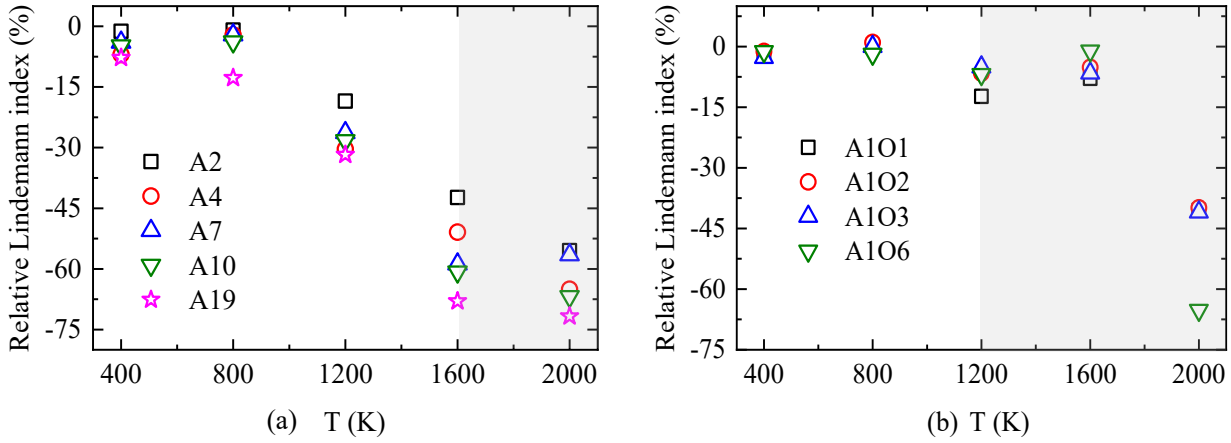

Fig. 10. Effect of coke adsorption on catalyst crystallinity of outer shell compared with the corresponding isothermal nanocrystal melting process, characterised by relative Lindemann index; grey area indicates seeping occurrence.

5 Conclusions

In order to attenuate the coke deposition and the resulting deactivation in biomass thermochemical catalytic conversion, a series of ReaxFF MD system is constructed to model the lignin pyrolysis process and to reveal the catalyst deactivation mechanism at different operating temperatures. The main conclusion includes:

The equilibrated system after 20 K/ps ratio temperature ramp (800 K-3000 K) in production run showed similarity of mass reduction trend compared with our TG experiments (423 K-1173 K). The coke surrogate models (*i.e.*, PAH and oxygenated aromatics) are proposed based on the identified molecular structure to reflect the molecular size and oxygen contents in practical coke respectively.

The Ni nanocatalyst surface thermal instability is investigated *via* the temperature dependence of Lindeman index over different layers. Outer shell of the 4 nm nanocrystal starts to show disorder and coordination number distribution modification when temperature is higher than 1200 K.

Isothermal ReaxFF MD system of a centred Ni nanocrystal surrounded by coke surrogate molecules is constructed to reveal the mechanism behind the chemisorption and physisorption at different temperature (400 K-2000 K). It is observed that adsorption is a complex process coupling the molecular collision dynamics (*e.g.*, benzene desorbs after trapped by the nanocrystal), thermal dynamics (*e.g.*, medium PAH like pyrene undergo dimerization and physical nucleation before adsorption at low temperature of 400 K) and kinetics (*e.g.*, surface reaction of benzenehexol and the subsequent desorption of intermediates at high temperature above 1200 K).

In comparison with the isothermal melting of nanocrystal, surface chemisorption is observed to facilitate the preserve of nanocatalyst crystallinity owing to the covalent bond prohibiting the mobility of surface atoms. Seeping of surface reaction intermediates at 1600 K and 2000 K into the inner layer of nanocrystal is adverse to catalyst regeneration.

6 References

[1] Transport Biofuels, https://www.iea.org/reports/transport-biofuels, [accessed on 30 April 2021] IEA, 2020.

[2] C. Li, X. Zhao, A. Wang, G.W. Huber, T. Zhang. Catalytic transformation of lignin for the production of chemicals and fuels. Chemical Reviews. 2015;115:11559-11624.

[3] W.J. Liu, W.W. Li, H. Jiang, H.Q. Yu. Fates of chemical elements in biomass during its pyrolysis. Chemical Reviews. 2017;117:6367-6398.

[4] M. Sharifzadeh, M. Sadeqzadeh, M. Guo, T.N. Borhani, N.M. Konda, M.C. Garcia, *et al*. The multi-scale challenges of biomass fast pyrolysis and bio-oil upgrading: Review of the state of art and future research directions. Progress in Energy and Combustion Science. 2019;71:1-80.

[5] A. Molino, S. Chianese, D. Musmarra. Biomass gasification technology: The state of the art overview. Journal of Energy Chemistry. 2016;25:10-25.

[6] A. Ochoa, J. Bilbao, A.G. Gayubo, P. Castaño. Coke formation and deactivation during catalytic reforming of biomass and waste pyrolysis products: A review. Renewable and Sustainable Energy Reviews. 2020;119:109600.

[7] L. Cheng, Z. Wu, Z. Zhang, C. Guo, N. Ellis, X. Bi, *et al*. Tar elimination from biomass gasification syngas with bauxite residue derived catalysts and gasification char. Applied Energy. 2020;258:114088.

[8] J. Li, J. Tao, B. Yan, K. Cheng, G. Chen, J. Hu. Microwave reforming with char-supported Nickel-Cerium catalysts: A potential approach for thorough conversion of biomass tar model compound. Applied Energy. 2020;261:114375.

[9] M. Hervy, E. Weiss-Hortala, D.P. Minh, H. Dib, A. Villot, C. Gerente, *et al*. Reactivity and deactivation mechanisms of pyrolysis chars from bio-waste during catalytic cracking of tar. Applied Energy. 2019;237:487-499.

[10] X. Hu, C. Lievens, D. Mourant, Y. Wang, L. Wu, R. Gunawan, *et al*. Investigation of deactivation mechanisms of a solid acid catalyst during esterification of the bio-oils from mallee biomass. Applied energy. 2013;111:94-103.

[11] A. Arregi, M. Amutio, G. Lopez, J. Bilbao, M. Olazar. Evaluation of thermochemical routes for hydrogen production from biomass: A review. Energy Conversion and Management. 2018;165:696-719.

[12] B.M. Murphy, B. Xu. Foundational techniques for catalyst design in the upgrading of biomass-derived multifunctional molecules. Progress in Energy and Combustion Science. 2018;67:1-30.

[13] C.H. Bartholomew. Mechanisms of catalyst deactivation. Applied Catalysis A: General. 2001;212:17-60.

[14] X. Gao, Z. Wang, J. Ashok, S. Kawi. A comprehensive review of anti-coking, anti-poisoning and anti-sintering catalysts for biomass tar reforming reaction. Chemical Engineering Science: X. 2020;7:100065.

[15] A. Arregi, G. Lopez, M. Amutio, M. Artetxe, I. Barbarias, J. Bilbao, *et al*. Role of operating conditions in the catalyst deactivation in the in-line steam reforming of volatiles from biomass fast pyrolysis. Fuel. 2018;216:233-244.

[16] A. Ochoa, B. Aramburu, B. Valle, D.E. Resasco, J. Bilbao, A.G. Gayubo, *et al*. Role of oxygenates and effect of operating conditions in the deactivation of a Ni supported catalyst during the steam reforming of bio-oil. Green Chemistry. 2017;19:4315-4333.

[17] C. Montero, A. Ochoa, P. Castaño, J. Bilbao, A.G. Gayubo. Monitoring Ni^0 and coke evolution during the deactivation of a $Ni/La_2O_3–\alpha Al_2O_3$ catalyst in ethanol steam reforming in a fluidized bed. Journal of Catalysis. 2015;331:181-192.

[18] C. Montero, A. Remiro, B. Valle, L. Oar-Arteta, J. Bilbao, A.G. Gayubo. Origin and nature of coke in ethanol steam reforming and its role in deactivation of $Ni/La_2O_3–\alpha Al_2O_3$ catalyst. Industrial & Engineering Chemistry Research. 2019;58:14736-14751.

[19] A.M. Lattanzi, M.B. Pecha, V.S. Bharadwaj, P.N. Ciesielski. Beyond the effectiveness factor: Multi-step reactions with intraparticle diffusion limitations. Chemical Engineering Journal. 2020;380:122507.

[20] B.D. Adkins, Z. Mills, J. Parks II, M.B. Pecha, P.N. Ciesielski, K. Iisa, *et al*. Predicting thermal excursions during in situ oxidative regeneration of packed bed catalytic fast pyrolysis catalyst. Reaction Chemistry & Engineering. 2021;6:888-904.

[21] M.B. Pecha, K. Iisa, M. Griffin, C. Mukarakate, R. French, B. Adkins, *et al*. *Ex situ* upgrading of pyrolysis vapors over $PtTiO_2$: extraction of apparent kinetics via hierarchical transport modeling. Reaction Chemistry & Engineering. 2021;6:125-137.

[22] Y. Zhang, H. He, Y. Liu, Y. Wang, F. Huo, M. Fan, *et al*. Recent progress in theoretical and computational studies on the utilization of lignocellulosic materials. Green Chemistry. 2019;21:9-35.

[23] P.N. Ciesielski, M.B. Pecha, A.M. Lattanzi, V.S. Bharadwaj, M.F. Crowley, L. Bu, *et al*. Advances in multiscale modeling of lignocellulosic Biomass. ACS Sustainable Chemistry Engineering. 2020;8:3512-3531.

[24] H. Zhu, S. Zhu, Z. Jia, S. Parvinian, Y. Li, O. Vaaland, *et al*. Anomalous scaling law of strength and toughness of cellulose nanopaper. Proceedings of the National Academy of Sciences. 2015;112:8971-8976.

[25] B. Lindner, L. Petridis, R. Schulz, J.C. Smith. Solvent-driven preferential association of lignin with regions of crystalline cellulose in molecular dynamics simulation. Biomacromolecules. 2013;14:3390-3398.

[26] J. Ding, G. Pan, L. Du, J. Lu, W. Wang, X. Wei, *et al*. Molecular dynamics simulations of the local structures and transport properties of Na_2CO_3 and K_2CO_3. Applied Energy. 2018;227:555-563.

[27] X. Nie, Z. Du, L. Zhao, S. Deng, Y. Zhang. Molecular dynamics study on transport properties of supercritical working fluids: Literature review and case study. Applied Energy. 2019;250:63-80.

[28] F.J. Keil. Molecular modelling for reactor design. Annual Review of Chemical and Biomolecular Engineering. 2018;9:201-227.

[29] S. Wang, G. Dai, H. Yang, Z. Luo. Lignocellulosic biomass pyrolysis mechanism: a state-of-the-art review. Progress in Energy and Combustion Science. 2017;62:33-86.

[30] M.R. Barr, M. Volpe, A. Messineo, R. Volpe. On the suitability of thermogravimetric balances for the study of biomass pyrolysis. Fuel. 2020;276:118069.

[31] A. Batuer, D. Chen, X. He, Z. Huang. Simulation methods of cotton pyrolysis based on ReaxFF and the influence of volatile removal ratio on volatile evolution and char formation. Chemical Engineering Journal. 2021;405:126633.

[32] S. Monti, P. Srifa, I. Kumaniaev, J.S. Samec. ReaxFF simulations of lignin fragmentation on a palladium-based heterogeneous catalyst in methanol-water solution. The Journal of Physical Chemistry Letters. 2018;9:5233-5239.

[33] C. Ashraf, A.C. van Duin. Extension of the ReaxFF combustion force field toward syngas combustion and initial oxidation kinetics. The Journal of Physical Chemistry A. 2017;121:1051-1068.

[34] H. Kwon, S. Shabnam, A.C. van Duin, Y. Xuan. Numerical simulations of yield-based sooting tendencies of aromatic fuels using ReaxFF molecular dynamics. Fuel. 2020;262:116545.

[35] Z. Chen, W. Sun, L. Zhao. Initial mechanism and kinetics of diesel incomplete combustion: ReaxFF molecular dynamics based on a multicomponent fuel model. The Journal of Physical Chemistry C. 2019;123:8512-8521.

[36] J.E. Mueller, A.C. van Duin, W.A. Goddard III. Application of the ReaxFF reactive force field to reactive dynamics of hydrocarbon chemisorption and decomposition. The Journal of Physical Chemistry C. 2010;114:5675-5685.

[37] J.E. Mueller, A.C. van Duin, W.A. Goddard III. Development and validation of ReaxFF reactive force field for hydrocarbon chemistry catalyzed by nickel. The Journal of Physical Chemistry C. 2010;114:4939-4949.

[38] A. Beste. ReaxFF study of the oxidation of lignin model compounds for the most common linkages in softwood in view of carbon fiber production. The Journal of Physical Chemistry A. 2014;118:803-814.

[39] A. Chatzigoulas, K. Karathanou, D. Dellis, Z. Cournia. NanoCrystal: A Web-Based Crystallographic Tool for the Construction of Nanoparticles Based on Their Crystal Habit. Journal of Chemical Information and Modeling. 2018;58:2380-2386.

[40] Q. Jiang, H. Lu, M. Zhao. Modelling of surface energies of elemental crystals. Journal of Physics: Condensed Matter. 2004;16:521.

[41] Q. Mao, A.C. van Duin, K.H. Luo. Formation of incipient soot particles from polycyclic aromatic hydrocarbons: a ReaxFF molecular dynamics study. Carbon. 2017;121:380-388.

[42] Q. Mao, D. Hou, K.H. Luo, X. You. Dimerization of polycyclic aromatic hydrocarbon molecules and radicals under flame conditions. The Journal of Physical Chemistry A. 2018;122:8701-8708.

[43] T. Zhang, X. Li, X. Qiao, M. Zheng, L. Guo, W. Song, *et al*. Initial mechanisms for an overall behavior of lignin pyrolysis through large-scale ReaxFF molecular dynamics simulations. Energy & Fuels. 2016;30:3140-3150.

[44] S. Plimpton. Fast parallel algorithms for short-range molecular dynamics. Journal of Computational Physics. 1995;117:1-19.

[45] A. Stukowski. Visualization and analysis of atomistic simulation data with OVITO-the Open Visualization Tool. Modelling Simulation in Materials Science and Engineering. 2009;18:015012.

[46] D. Hong, T. Si, X. Guo. Insight into the calcium carboxylate release behavior during Zhundong coal pyrolysis and combustion. Proceedings of the Combustion Institute. 2020.

[47] Y. Qian, J. Zhan, D. Lai, M. Li, X. Liu, G. Xu. Primary understanding of non-isothermal pyrolysis

behavior for oil shale kerogen using reactive molecular dynamics simulation. International Journal of Hydrogen Energy. 2016;41:12093-12100.

[48] J.A. Okolie, R. Rana, S. Nanda, A.K. Dalai, J.A. Kozinski. Supercritical water gasification of biomass: a state-of-the-art review of process parameters, reaction mechanisms and catalysis. Sustainable Energy & Fuels. 2019;3:578-598.

[49] M.D. Argyle, C.H. Bartholomew. Heterogeneous catalyst deactivation and regeneration: a review. Catalysts. 2015;5:145-269.

[50] E.C. Neyts, A. Bogaerts. Numerical study of the size-dependent melting mechanisms of nickel nanoclusters. The Journal of Physical Chemistry C. 2009;113:2771-2776.

[51] A. Chernyshev. Effect of nanoparticle size on the onset temperature of surface melting. Materials Letters. 2009;63:1525-1527.

[52] Z. Li, H. Wang. Gas-nanoparticle scattering: A molecular view of momentum accommodation function. Physical Review Letters. 2005;95:014502.